PAPER

Check for updates

Bifunctionally active nanosized spinel cobalt nickel sulfides for sustainable secondary zinc–air batteries: examining the effects of compositional tuning on OER and ORR activity†

Yijie Xu, [ID] [ab] Afriyanti Sumboja, [cd] Yun Zong [ID] *[b] and Jawwad A. Darr*[a]

A range of compositionally-tuned nanosized cobalt nickel sulfides (<15 nm) were prepared *via* a sustainable continuous hydrothermal flow synthesis (CHFS) method and evaluated as electrocatalysts for the oxygen reduction reaction (ORR) and oxygen evolution reaction (OER) as well as air cathodes in rechargeable zinc–air batteries. The electrochemical study results showed that with the nominal composition of $Ni_{1.5}Co_{1.5}S_4$, the cobalt nickel sulfide powder possesses an OER activity on a par with that of RuO_2, while displaying superior cycling stability (>125 cycles) and a decent power density of 87 mW cm^{-2} at 150 mA cm^{-2} in zinc–air batteries. The electrochemical study of the series of cobalt nickel sulfides made herein suggests that a high electronic conductivity is responsible for the high bifunctional performance, with Ni(III) being identified as a contributor to the OER, while Co(II) and Ni(II) are identified as contributors to the ORR activity. These cathode materials would be highly suitable for safe, sustainable, and long-life zinc–air secondary batteries.

Introduction

The concern over accelerated global warming and its relationship to the consumption of fossil fuels has shifted energy use to sustainable sources.[1,2] With most economical and safe alternative energy sources being intermittent in nature, there is a growing demand to employ grid-scale energy storage solutions using inexpensive rechargeable batteries as the basic units. Zinc–air batteries have emerged as a promising choice for such applications due to their high energy density, low cost, environmental benignity, and excellent safety features inherited from the aqueous electrolyte (non-flammable) and being an open system (no pressure build-up to risk an explosion).[3,4] Typically, a zinc–air battery consists of a metallic zinc anode and a catalytic air-cathode placed opposite to each other in an alkaline electrolyte. During discharge, oxygen molecules are reduced to hydroxide ions, OH^- (*i.e.* oxygen reduction reaction, or ORR), on the cathode with zinc being oxidized to Zn^{2+} at the anode side to dissolve into the electrolyte. The processes are reversed during charge, where oxygen gas is evolved from OH^- (*i.e.* oxygen evolution reaction, or OER) at the air-cathode surface with zinc being plated back onto the anode. Theoretically, the battery delivers an equilibrium voltage of 1.65 volts; however this is often notably lower due to the overpotential primarily on the air-cathode. In addition, the conversions between oxygen molecules and hydroxide ions (ORR and OER) are known to display sluggish kinetics, leading to a poor rate capability of zinc–air batteries. Incorporating a bifunctional catalyst with the ability to facilitate both the ORR and OER on the air-cathode is a well-established strategy to tackle these issues.[3] With high bifunctional catalytic activities, a catalyst can be anticipated to greatly improve the kinetics of ORR and OER catalyses involving multi-electron transfer,[5,6] lowering cathode overpotentials and thus improving the round-trip energy efficiency of zinc–air batteries.

Precious metal-based catalysts often possess prominent OER or ORR catalytic activity, *e.g.* RuO_2 or Ir/C for the OER and Pt/C for the ORR. However, their scarcity and high cost make them commercially unviable for large-scale applications.[3,5] Inexpensive alternatives to precious metals

[a] Department of Chemistry, University College London, 20 Gordon Street, London WC1H 0AJ, UK. E-mail: j.a.darr@ucl.ac.uk
[b] Institute of Materials Research and Engineering (IMRE), A*STAR (Agency for Science, Technology and Research), 2 Fusionopolis Way, Innovis #08-03, 138634, Singapore. E-mail: y-zong@imre.a-star.edu.sg
[c] Material Science and Engineering Research Group, Faculty of Mechanical and Aerospace Engineering, Institut Teknologi Bandung, Jl. Ganesha 10, Bandung 40132, Indonesia
[d] National Centre for Sustainable Transportation Technology (NCSTT), Jl. Ganesha 10, Bandung 40132, Indonesia
† Electronic supplementary information (ESI) available. See DOI: 10.1039/c9cy02185j

This journal is © The Royal Society of Chemistry 2020

Catal. Sci. Technol., 2020, **10**, 2173–2182 | **2173**

have emerged as capable substitutes, including those based on earth-abundant transition metal compounds.[6–9] These compounds are of interest due to their low cost and steadily improving catalytic activities. Strategies to improve catalytic activities include: 1) introducing nanostructured conductive additives or supports to promote the electron transfer; 2) enlarging the electrochemical active surface area *via* chemical activation to populate the exposed catalytically active sites; 3) doping with hetero-atoms to fine-tune the localized chemical and electronic environment.[10]

Transition metal oxides and hydroxides have exhibited good OER activity, while their sulfide, selenide, nitride, and phosphide counterparts have demonstrated potential as ORR catalysts.[11–16] Transition metal chalcogenides, particularly the ternary ones, have demonstrated desirable electrocatalytic activities,[12,17] benefitting from the inter-element synergistic coupling.[5,9] For instance, cobalt nickel chalcogenide spinels exhibited notably improved activities over their individual monometallic counterparts in the catalysis of methane oxidation or water oxidation.[18,19]

Spinel bimetallic sulfides (*e.g.* $NiCo_2S_4$) are also of interest for oxygen electrocatalysis, thanks to their rich multivalent oxidation state chemistry, good chemical and thermal stability, high electronic conductivity, and rich exposed octahedral active sites.[7,18,20,21] $NiCo_2S_4$ can be synthesized in various morphologies and has been used in other applications such as an active material in supercapacitors, lithium-ion batteries, dye-sensitized solar batteries, and catalysis including the ORR, OER and hydrogen evolution reaction (HER).[22–27] These $NiCo_2S_4$ nanostructures, such as spheres and wires, have all exhibited good bifunctional OER and ORR activity,[5,6,8,9,12,28–30] which may be further enhanced by improving electron transfer *via* the engineering of surface morphology, incorporating highly conductive support materials, and doping with selected tertiary atoms.[5,31–37]

Previous studies show that $NiCo_2S_4$ possesses a mixed-valence redox chemistry.[5,12,18] However, it remains largely not understood how individual cobalt and nickel cations affect the electrocatalytic performance of $NiCo_2S_4$.[12,17] The intrinsic filling restrictions of the spinel structure, fortunately, allow the contribution of each cationic species with specific occupancy in the bimetallic spinels to be distinguished and correlated to the catalytic activities.[38–40] This was achieved by varying the ratio of two metallic precursors in the synthesis, and relating the differences in the composition to their catalytic activities. The obtained knowledge can be used to design electrocatalysts for optimum catalytic activity.[38,41,42] An emphasis here is to adopt scalable and reproducible routes for large-scale manufacture viability.

Amongst various nanoparticulate oxide manufacture processes, the continuous hydrothermal flow synthesis (CHFS) method is a fast and scalable synthetic approach with good control and consistency over particle properties.[43] In a typical CHFS reaction, such as that developed by the authors, an aqueous metal salt feed at ambient temperature and high pressure is rapidly mixed with a feed of supercritical water (typically at 450 °C and a pressure of 24.1 MPa) in a specially engineered turbulent mixer. The sudden change in reaction conditions experienced by the metal salts results in rapid supersaturation and formation of inorganic nanocrystals *via* a complex set of chemical reactions, including hydrolysis, degradation and dehydration processes.[44] CHFS-made products include homometallic oxides,[45] metal phosphates,[46] nitrides (*via* further nitration of CHFS-made metal oxide nanoparticles),[47] and sulfides,[48] as well as heterometallic oxides (*e.g.* lanthanum nickelates *via* a solid state reaction of CHFS-made nanoparticles).[49]

Herein, the authors synthesized phase pure nickel cobalt sulfide spinel nanomaterials ($Ni_xCo_yS_4$) with varied compositions using CHFS and then evaluated their electrochemical performance as bifunctional electrocatalysts and in zinc–air batteries. The total metal content in the catalysts was quantified using inductively coupled plasma optical emission spectrometry (ICP-OES), X-ray fluorescence (XRF) spectroscopy, and energy-dispersive X-ray spectroscopy (EDS), whilst the ratios of $Ni(III):Ni(II)$ and $Co(III):Co(II)$ were determined using X-ray photoelectron spectroscopy (XPS). By varying the proportions of different cations in the nominal compounds Co_2NiS_4, $NiCo_2S_4$, and $Ni_{1.5}Co_{1.5}S_4$ and examining their electrochemical properties, the individual contributions of the respective metals with different valence states to the OER and ORR catalytic activity can be evaluated.

Experimental

Synthesis of nickel cobalt-sulfide nanoparticles

Spinel nickel cobalt sulfide nanoparticles with specific compositions were synthesised using a CHFS reactor. The laboratory scale CHFS reactor used herein has a similar design to the pilot scale CHFS described previously,[50] but at *ca.* one fifth scale of the latter. The exact setup can be viewed in Fig. S1.†

Briefly, the CHFS process can be described as follows: the laboratory-scale CHFS reactor consisted of four identical pumps (Primeroyal K, Milton Roy, France) to supply independent feeds, which were pressurised to 24.1 MPa. Nanoparticles were formed in a double confined jet mixer (CJMS, patent no. US 9192901) arrangement.[51–54] The first mixer was a 3/8 inch CJM, whilst the second was also a 3/8 inch mixer as shown in Fig. S1;† both were designed to reduce blockages in flow and made from off-the-shelf Swagelok parts, as described in earlier publications, and connected *via* a Swagelok 3/8 to 3/16 inch reducer.[55] In the process, an aqueous solution of 2 M thiourea was fed at a flow rate of 40 mL min^{−1} by both pumps 2 & 3 each (to give an overall rate of 80 mL min^{−1}), and brought into contact with an 80 mL min^{−1} feed of supercritical water (P1) at *ca.* 450 °C and 24.1 MPa within the first 3/8 inch CJM (in order to initiate the breakdown of thiourea at a mixing temperature of *ca.* 330 °C). After *ca.* 4 seconds, the slurry from this mixture was brought into contact with an ambient temperature feed of cobalt and nickel nitrates (40 mL min^{−1},

2174 | *Catal. Sci. Technol.*, 2020, **10**, 2173–2182

This journal is © The Royal Society of Chemistry 2020

total metal concentration 0.1 M), in a second 3/8 inch CJM (mixing temperature = 187 °C) to facilitate rapid nanoparticle formation.[51,56–58]

Special care was taken to ensure sufficient ventilation of the process as the reactions were likely to produce hydrogen sulfide, a toxic and pungent gas. The newly formed nanomaterials were then cooled down in the process using an enlarged pipe-in-pipe heat exchanger to facilitate their growth into nanoparticles, before passing through a back-pressure regulator to an outlet at *ca.* 40 °C. After this process, the black nanoparticle laden slurry was collected and allowed to sediment under gravity, before being cleaned by washing briefly in pH 8 ammonia solution. The resulting wet solids were then freeze-dried (Virtis Genesis 35XL) by warming the samples from −60 °C to 25 °C for 24 h under a vacuum of <13.3 Pa, yielding free-flowing powders. The spinel sulfides were named according to their Ni and Co salt compositions during their synthesis, such as NC11, NC13, or NC31, respectively. For instance, NC11 denotes the sample prepared by using a solution containing a total concentration of 0.1 M Co and Ni salts, with the molar ratio of Ni to Co being 1:1. The same applies to NC13 and NC31, except for NiS_2 prepared in the absence of a cobalt precursor.

Material characterization

The powder X-ray diffraction (XRD) data of the samples were collected over the 2θ range of 2 to 45° at a step size of 0.5° with 10 s intervals on a Stöe diffractometer using Mo-Kα radiation (λ = 0.7093 Å). A high-resolution transmission electron microscope (HR-TEM, Jeol JEM 2100, fitted with a LaB_6 filament) was used to observe the fine features of the particles for morphology, size and interlayer spacing, with their elemental composition being examined *via* the attached energy-dispersive X-ray spectrometer (EDS). A Gatan Orius digital camera was employed to capture digital images of the sulfide samples prepared by ultrasonically dispersing the powder in >99.5% pure methanol (EMPLURA, Darmstadt, Germany) and pipetting onto a copper film grid (300 mesh Agar Scientific, Stansted, UK). Chemical bonding and valence information at the sample surface was determined by X-ray photoelectron spectroscopy (XPS) (Thermo Scientific Theta Probe) with Al-Kα (hv = 1484.6 eV) radiation. High-resolution regional scans for Co 2p, Ni 2p, O 1s, C 1s, and S 2p were conducted at 50 eV, with the XPS data fitted using CasaXPS™ software (Version 2.3.16). The adventitious C 1s peak at 284.7 eV was used for the calibration of the spectra. Elemental inductively coupled plasma with optical emission spectroscopy (ICP-OES) (Perkin Elmer Optima 5300DV) analysis was used to quantify the Ni/Co ratio after the samples were digested in concentrated HNO_3. The Brunauer–Emmet–Teller (BET) surface area of the powders were measured using the adsorption/desorption of liquid N_2 on a Hyden BET instrument. The sample was first degassed at 150 °C (for 12 h) under a flow of nitrogen gas prior to the measurement. X-Ray fluorescence (XRF) spectrometry data of the nickel cobalt sulfide were collected on a Brüker M4 Micro XRF spectrometer using a 30 W Rh source.

Electrochemical characterization

The catalytic performance of all the samples was examined on a potentiostat (Autolab model PGSTAT302N), using a three-electrode set-up incorporating a rotating-disk electrode (RDE) in 0.1 M or 1 M KOH for the ORR and OER (Model RDE-2, Metrohm AG, Herisau, Switzerland), respectively. For the ORR tests, the setup was continuously purged with O_2 gas, while for the OER tests the electrolyte was first saturated with O_2 gas to establish equilibrium. The reference and counter electrodes were an Ag/AgCl electrode (Model 6.0726, Metrohm AG, Herisau, Switzerland) and Pt foil (Model 3.109 Metrohm AG, Herisau, Switzerland), respectively. Catalyst inks were prepared from an 80:20 wt% mixture of active material and carbon black (Vulcan XC-72, Cabot, Alpharetta Georgia, USA), added into a mixture of 10 mL DI H_2O, isopropyl alcohol (IPA), and Nafion™ (10% solution, Sigma Aldrich, Dorset UK) solution at a mass ratio of 2.5:1:0.094, and sonicated for 30 minutes to achieve an active material concentration of 3.75 mg mL^{-1}. 10.68 μL of each catalyst ink was drop-cast onto a polished glassy carbon electrode to give a loading of 0.1 mg cm^{-2}, and then air-dried for 30 min at ambient temperature. RuO_2 (99.9%, Sigma Aldrich, Dorset UK) and Pt/C (99.9%, Sigma Aldrich, Dorset UK) were also prepared into an electrode of similar loading each and used for electrocatalytic performance benchmarking.
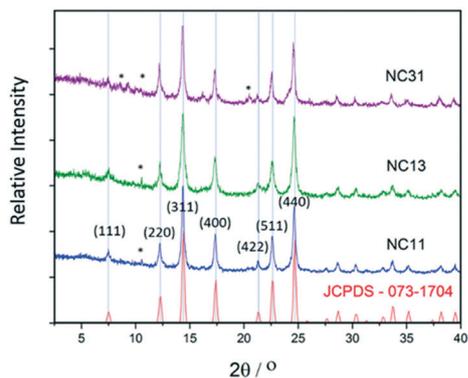
The performance of these electrocatalysts was further evaluated in an in-house customized Zn–air battery on a battery tester (Neware, model V5, Shenzen Neware Technology Company, China). To prepare the air-cathode, each of the nickel cobalt sulfide dispersions was pipetted onto a piece of carbon paper to achieve an active material loading of *ca.* 1.5 ± 0.1 mg cm^{-2}. It was then coupled with a polished 70 × 60 × 10 mm Zn plate anode, using a 6.0 M KOH aqueous solution containing 0.1 M $Zn(O_2CCH_3)_2$ as the electrolyte. A titanium mesh (Ti, 80 mesh, Alfa Aesar, Haverhill Massachusetts, USA) was applied as the cathode current collector, with a Teflon-coated carbon paper backing layer (SIGRACELL, SGL Carbon, Weisbaden, Germany) to prevent electrolyte leakage or cell flooding under high humidity conditions. The area of the air-cathode exposed to the electrolyte and air was *ca.* 0.79 cm^2.

Results & discussion

Physical characterization

The powder X-ray diffraction patterns of the nickel cobalt sulfide samples are shown in Fig. 1, together with the reference pattern for $NiCo_2S_4$ (JCPDS 073-1704), which is indistinguishable with that for $CoNi_2S_4$ (JCPDS 073-1297) due to similar ionic radii of cobalt and nickel.[59] The patterns of the three nickel cobalt sulfides with varied Ni/Co ratios all display characteristic peaks at 2 theta of 7.5° (111), 12.3° (220), 14.4° (311), 17.4° (400), 21.3° (422), 22.6° (511), and

This journal is © The Royal Society of Chemistry 2020

Catal. Sci. Technol., 2020, **10**, 2173–2182 | **2175**

Fig. 1 XRD patterns of the as-synthesized nickel cobalt sulfides, shown alongside the JCPDS pattern 073–1704 (space group $Fd\bar{3}m$) for $NiCo_2S_4$ (red). Impurity peaks, attributed to NiS_2 and CoO_2, are marked with an asterisk (*). The tiny peak at 2 theta = 10.7° for all the samples is from CoO_2 impurity, with two more peaks at 6.2° and 20.7° for NC31 arising from NiS_2 impurity.

24.7° (440), respectively. The tiny peak at 10.7° for all the samples is likely from CoO_2 impurity (with two more peaks at 6.2° and 20.7° for NC31 arising from NiS_2 impurity). CoO_2 is likely segregated in these samples, and not known to be intrinsically active for oxygen electrocatalysis. Its analogue $NiCoO_2$ has an electrocatalytic activity for the ORR and OER, albeit poorer than that of $NiCo_2S_4$, while it is absent based on the XRD patterns.[60] The characterization of the as-made NiS_2 sample is shown in Fig. S5,† which shows broad agreement with the reference pattern for NiS_2.

In a typical spinel structure, *e.g.* for $NiCo_2S_4$, there are cubic close-packed S^{2-} anions with eight tetrahedral sites and four octahedral sites occupied by Co(III) and Ni(II) cations, respectively, in an $Fd\bar{3}m$ space group.[12,61] Nevertheless, powder neutron diffraction studies showed that the cations of spinel $CoNi_2S_4$ occupied these sites in a reverse manner, *i.e.* Ni(III) and Co(II) in the tetrahedral sites and octahedral sites, respectively.[61,62] This makes it difficult to use XRD data to distinguish between $CoNi_2S_4$, $NiCo_2S_4$ and other possible immediate states, *e.g.* the mixed metal sulfide samples herein.

Transmission electron microscopy (TEM) images showed the nickel cobalt sulfide samples as agglomerated nanostructures (Fig. 2). High-resolution TEM (HRTEM)
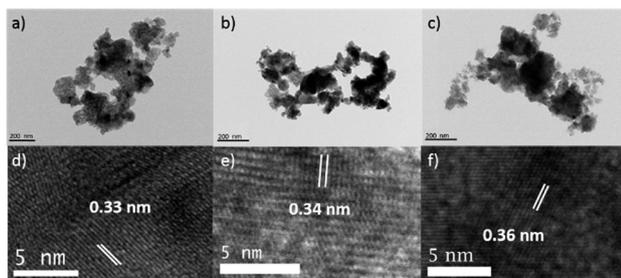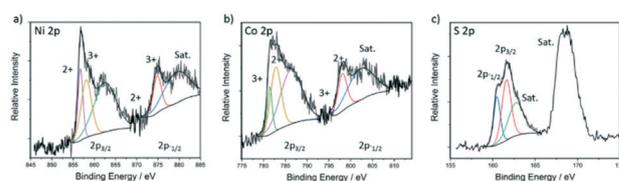
revealed the *d* spacings of (440) planes for NC13, NC11, and NC31 to be *ca.* 0.33, 0.34, and 0.36 nm, respectively, similar to those reported by Kim and Liang for $NiCo_2S_4$.[63,64] The BET surface areas were similar for NC13, NC11, and NC31, at *ca.* 15, 12, and 16 m^2 g^{-1}, respectively.[63]

The composition and chemical valence states of the nickel cobalt sulfides were characterized by X-ray photoemission spectroscopy (XPS), confirming the presence of cobalt, nickel, and sulfur in all three samples. Fig. 3 shows the fitted Co 2p, Ni 2p, and S 2p spectra of NC11. The deconvoluted two spin–orbital doublets may come from M(II) and M(III) of both metals along with their shake-up satellites. The peaks of these nickel cobalt sulfides are almost at the same positions but differ in peak intensities. For Co 2p, the doublet pairs at 781.4 and 778.0 eV and at 792.9 and 797.3 eV are assigned to its 2p3/2 and 2p1/2 state, respectively. For Ni 2p, the doublet pair at 856.4 and 852.8 eV accounts for 2p3/2, with the peak of 2p1/2 being a singlet at 874.1 eV. S 2p showed peaks at 161.3 and 162.6 eV for 2p3/2 and 2p1/2, respectively, in agreement with those of reported transition-metal sulfides.[21,65] Further compositional information was obtained using XRF, EDS and ICP-OES, and the data are summarized in Table S1.† With XPS and EDS revealing the composition close to the surfaces, XRF and ICP-OES reflect that of the overall bulk samples. The XRD patterns and the composition data in tandem suggested the formulas of NC13, NC11 and NC31 as $Ni_{0.8}Co_{2.2}S_4$, $Ni_{1.5}Co_{1.5}S_4$ and $Ni_{2.2}Co_{0.8}S_4$, respectively.

The XPS and EDS data suggested sulfur deficiency at the surfaces of these samples. The presence of surface anionic vacancies has been shown to enhance the OER catalytic performance of perovskites.[66–68] On the other hand, surface nickel and cobalt cations of different oxidation states (II or III) may affect the catalytic activities by varied binding strength to oxygen species. Hence, a detailed understanding of the surface composition of the samples is crucial. The portion of each cation with different oxidation states in the three nickel cobalt sulfides was calculated from the XPS data and is summarized in Table 1, with the ratios of each cation pair of different oxidation states given in Table S2.† With similar BET surface areas for the three nickel cobalt sulfides, it is reasonable to associate the catalytic performance of each sample with its proportional cationic composition.

Unsurprisingly, the two oxidation states were found to co-exist for both nickel and cobalt in the samples, echoing the powder neutron diffraction data reported by Nakagawa.[61] The concentration of a specific cation is proportional to its

Fig. 2 TEM and HRTEM images of nickel cobalt sulfides. a and d) NC13; b and e) NC11; c and f) NC31.

Fig. 3 XPS spectra of NC11. a) Ni 2p, b) Co 2p, and c) S 2p.

2176 | *Catal. Sci. Technol.*, 2020, **10**, 2173–2182

This journal is © The Royal Society of Chemistry 2020

Table 1 Calculated specific relative metal ion compositions of the three nickel cobalt sulfides

	NC31/at%	NC11/at%	NC13/at%
Co(II)	31	42	47
Co(III)	5	7	24
Ni(II)	3	12	9
Ni(III)	61	39	20

content in the precursors, with all the samples showing comparably higher concentrations of Co(II) and Ni(III). Such a pattern was also observed by Zhang *et al.* in their $Ni_{1.5}Co_{1.5}S_4$ prepared *via* a two-step batch hydrothermal method.[69] The co-existence of oxidation states in both sites is quite common for nickel cobalt oxides, as reported previously in XPS, XANES, and magnetic moment studies.[6,70,71] Among the three samples, NC31 was found to be rich in Ni(III) (61 at%), NC13 has high cobalt content (*ca.* 71 at%), and NC11 shows equivalent proportions of nickel and cobalt with 39 at% of Ni(III) and 42 at% of Co(II), respectively. The results suggest comparable abilities of the two ionic species in occupying the octahedral or tetrahedral sites.[61] The characterization of the as-made NiS_2 sample is shown in Fig. S5b) and S5c),† displaying a significantly higher percentage of Ni(III) over NI(II), at 15% to 85%, respectively.

Electrochemical characterization

The nickel cobalt sulfides were further evaluated for their catalytic activities toward the OER in 1 M KOH on a rotating disc electrode (RDE) set-up (model GC50, MetroOhm, Switzerland) at a scan rate of 5 mV s^{-1}. In Fig. 4a, the linear sweep voltammetry (LSV) scan curves of the three samples
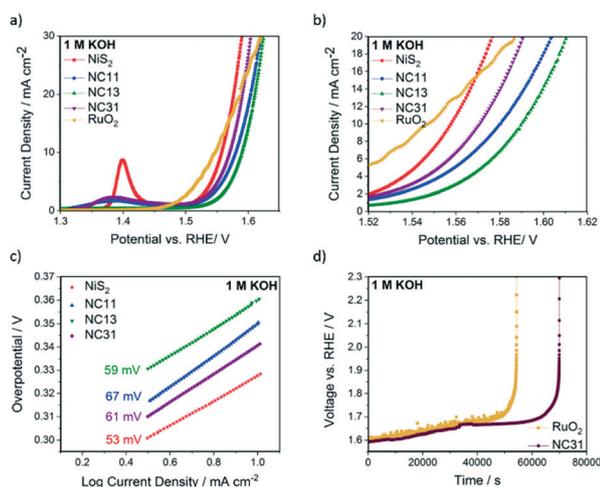

Fig. 4 OER catalytic activity of the nickel cobalt sulfides, using RuO_2 and NiS_2 as the benchmark and control samples, respectively. a) LSV curves. b) Close-up of Fig. 4a, showing the relative current densities at different voltages in closer detail. c) Tafel slopes derived from LSV curves. d) Stability tests of NC31 and RuO_2, measured at 10 mA cm^{-2}. All measurements were conducted in 1 M KOH at a rotating speed of 1600 rpm.

suggest the promotion of OER activity by higher nickel content, as NiS_2 and NC31 topped the OER activity with a current density of 10 mA cm^{-2} achieved at low overpotentials of 328 and 341 mV, respectively. In contrast, NC11 and NC13, both possessing lower overall nickel content, required overpotentials of 351 and 360 mV, respectively, in order to achieve the same current density. The variation of nickel and cobalt content clearly was able to change the OER performance of the resultant nickel cobalt sulfide. NC31 exhibited the highest current density (64 mA cm^{-2} at 1.63 V) and the lowest overpotential (341 mV) in the OER. This is likely attributed to it having the highest ratio of Ni(III), triple that of NC13, along with the highest overall nickel content. In comparison to sample NC13 with the lowest OER activity, sample NC31 also possessed a notably lower content of Ni(II) (3 *vs.* 9 at%) and Co(III) (5 *vs.* 24 at%). This suggests Ni(III) species as a key contributor to the OER catalytic activity. Oxidation peaks were also observed from 1.32 to 1.44 V, and were attributed to the Ni(II) to Ni(III) transition, as previously reported for nickel and nickel cobalt sulfides in the literature.[72,73]

NC31's overpotential required to achieve a current density of 10 mA cm^{-2} was comparable or even smaller than that of comparable literature reports including porous $NiCo_2S_4$ synthesized *via* a solvothermal method (337 mV), graphene oxide supported nitrogen-doped $NiCo_2S_4$ (470 mV) in 0.1 M KOH,[6] and $NiCo_2S_4$ nanowires supported on carbon cloth (340 mV) in 1 M KOH.[9] The OER activity of NC31 may be further improved if incorporated with high surface-area conductive supports, as proven in other reported material systems, such as nanowire $NiCo_2S_4$ mounted on nickel foam (10 mA cm^{-2} @ 260 mV in 1 M KOH),[5] graphydiene-supported $NiCo_2S_4$ (20 mA cm^{-2} @ 308 mV in 1 M KOH),[28] or $NiCo_2S_4$ on heterostructures of NiFe layered double hydroxides with a nickel foam support (60 mA cm^{-2} @ 201 mV in 1 M KOH).[70]

The higher OER activity of NiS_2 and NC31 is also reflected by their smaller Tafel slopes of 53 and 61 mV dec^{-1} (Fig. 4c), lower than that of a number of reported good OER catalysts, such as Co_3O_4 (74 mV dec^{-1}),[74] $CuCo_2O_4$ (65 mV dec^{-1}),[75] graphene-supported Co_3O_4 (67 mV dec^{-1}),[76] graphene-supported copper-based MOFs (65 mV dec^{-1}),[77] and nickel foam-supported NiSe (64 mV dec^{-1}).[78]
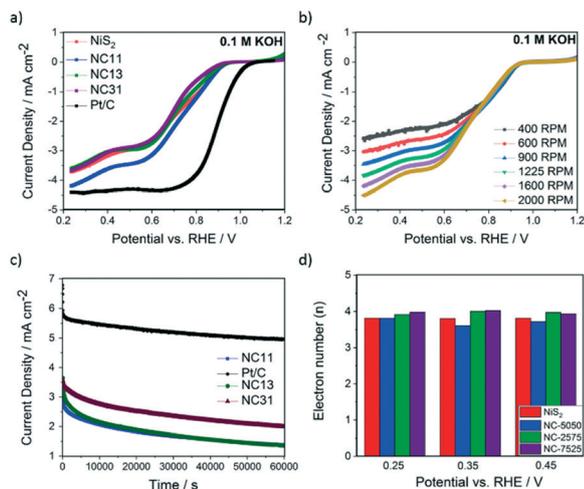
The electrochemical stability of NC31 was examined by chronopotentiometry, with the voltage to achieve a current density of 10 mA cm^{-2} being recorded over time. RuO_2 as the benchmark catalyst was also subjected to the same test. The results clearly showed the superiority of NC31 over RuO_2 in 1 M KOH electrolyte (Fig. 4d).

The ORR catalytic activities of the NCS samples were evaluated in 0.1 M KOH in the same setup (Fig. 5). Linear sweep voltammetry curves revealed essentially the same onset potentials of 0.93, 0.92, and 0.92 V for NC13, NC11, and NC31, respectively (measured *via* the tangent intersection method as demonstrated in Fig. S3 in the ESI†), comparable to those of NiS_2 (0.92 V) and $NiCo_2S_4$ reported previously.[6,8]

This journal is © The Royal Society of Chemistry 2020

Catal. Sci. Technol., 2020, **10**, 2173–2182 | **2177**

Fig. 5 Oxygen reduction reaction (ORR) activity tests. a) LSV curves of the samples measured at 1600 rpm and a scan rate of 5.0 mV s^{-1}, across a potential range of 0.2 to 1.2 V (*vs.* RHE). b) LSV curves of NC11 at a scan rate of 5.0 mV s^{-1} at different rotation rates. c) Long-term stability test data of NC11, NC13, NC31, and Pt/C, at a constant potential of 1.0 V (*vs.* RHE). d) Electron transport number per oxygen molecule for NiS$_2$, NC11, NC13, and NC31, calculated at three different potentials. All measurements were carried out in 0.1 M KOH.

The comparably higher ORR current density on NC11 than that on NC31 and NC13, according to XPS analysis, likely originated from its higher content of Ni(II) and Co(II). This is echoed by the fact that NiS$_2$, which exhibited a high level of Ni(II) and an absence of Co(II), displayed inferior ORR activity to the stoichiometric NiCo$_2$S$_4$, as observed in a previous literature study.[8] The less positive onset potentials and lower current density (*vs.* Pt/C) herein may be improved by increasing the surface area of the catalysts, or by incorporating other doped carbons, which was not undertaken in this work.[79]

The long-term stability of NC11 was examined *via* chronoamperometry in 0.1 M KOH, using Pt/C as the benchmark. A 50%, 52%, and 40% decrease in current density over 16 h was observed for NC11, NC13, and NC31, respectively, compared to a 13% loss for Pt/C over the same period. This suggests that a higher proportion of nickel enhances the long-term ORR stability. The ORR on these three nickel cobalt sulfides was shown to undergo 4-electron transfer dominated pathways, with NC31 and NC13 showing transfer of *ca.* 4 electrons per oxygen molecule. The value of *ca.* 3.7 for NC11 implied some co-occurrence of a two-electron transfer pathway in its catalyzed ORR, in which the produced detrimental hydroperoxide would corrode the carbon support in the air-cathode.[80] Improving the stability of transition metal-based bifunctional catalyst materials has been demonstrated in the literature through the use of graphitized carbons, although this was not explored in this study.[81]

The OER and ORR catalytic activities of these nickel cobalt sulfides can be associated with their conductivity, electronic structure, and the synergistic coupling effects between nickel and cobalt cations. NiCo$_2$S$_4$ is known to be highly conductive, *ca.* 100 times that of NiCo$_2$O$_4$, and up to 10^4 times higher than that of its monometallic counterparts, boosting its overall electrocatalytic activity.[21,82,83] A study by Xia *et al.* suggested metallic-like conduction in NiCo$_2$S$_4$ with a linear relationship between resistivity and temperature,[20] which has been linked to the Ni(II) cations in the t$_{2g}^4$e$_g^4$ high-spin configuration occupying the tetrahedral sites of the spinel structure.[12] The high conductivity was also partially ascribed to the lower bandgap of NiCo$_2$S$_4$ and the synergistic coupling between Co(II) and Ni(III) cations, resulting in p-type and n-type doping, respectively.[84,85] Hence, to promote the electronic conductivity of NC catalysts, a desirable approach would be to increase the Ni(III) content for maximized n-type (electron-rich) doping while reducing the Co(II) content for minimized p-type (electron-deficient) doping. This matched well with the OER activity trend in our NC catalysts (NC31–NC13), with the content of Co(II) decreasing and the Ni(III) content increasing. Also for ORR activity, NC11 with a comparable onset potential but a comparably higher current density featured a high amount of Ni(II) and Ni(II) cations, about 30% or 95% higher over that in NC13.

The notable contribution of Ni(III) to OER activity was reported by Wang *et al.* in a study using X-ray absorption scattering (XAS), in which Ni(III)-rich Ni–Co oxide compounds exhibited high OER activity and formed a stable OER cycle with their counter hydroxide species. This partially explains the high OER activity of our nickel-heavy NC31.[86] Another possible mechanism could be the conversion of Ni(III) to Ni(IV) prior to the OER, generating more attractive active sites for –OOH adsorption.[87,88] The mixed valences of each cation species would lower the activation energy of insertion-based electron transfer and enrich the active sites for reversible chemisorption of oxygen.[89] Additionally, NiCo$_2$S$_4$ is more flexible in structure due to the lower electronegativity of sulfur, allowing for reversible layer elongation and contraction within the intact structure which facilitates good electron transport.[18,84,90]

Suntivich *et al.* correlated the catalytic activities of spinel metal oxides to the e$_g$-orbital occupancy in the electronic structure of the metal cations at low-spin octahedral centres, which has also been found to hold true for spinel metal oxides.[91,92] Spinel materials with an e$_g$-orbital occupancy level of close to unity were found to favour electron transfer from the surface metal cations to the adsorbed intermediates. Consequently, it alters the energy of the rate determining step, with the occupancy value slightly higher or lower than unity favouring OER and ORR activity, respectively.[66,91] This attribute was successfully demonstrated by the Co(III), Co(II), and Ni(III) cations on the surface of nickel cobalt oxides. For NiCo$_2$S$_4$, the bulk state octahedral Co(III) sites were reported to adopt the less active t$_{2g}^6$e$_g^0$ configuration. However, anion vacancies on spinel particle surfaces can result in distortion into a square-pyramidal crystal field with an intermediate spin state of t$_{2g}^5$e$_g^1$, depending on the local coordination conditions.[91] Similarly, Ni(III) has been shown to adopt the

2178 | *Catal. Sci. Technol.*, 2020, **10**, 2173–2182

This journal is © The Royal Society of Chemistry 2020

favourable $t_{2g}^6 e_g^1$ state in more nickel-rich $CoNi_2S_4$.[66,91] As the lone electron in the e_g-orbital would enhance OER and ORR activities, a high content of the two cations is highly favourable.[12] Co(III) adopting an intermediate spin state may be partially responsible for the similar ORR activity of NC13 and NC31, despite the poorer conductivity of NC13.

The high ORR activity of NC11 is likely associated with its high conductivity and with the high content of Co(II) and Ni(II) cations. The partial doping of nickel into Co_3S_4 has been shown to improve the ORR kinetics,[6] with DFT studies suggesting the beneficial effect of larger size co-dopant cations in cobalt sulfides, e.g. Ni(II) [83 vs. 69 pm for Co(III)], which stretch both the Co(III)–O and adsorbate O–O bonds to facilitate intermediate formation and an improved ORR activity. This was also observed in spinel cobalt oxides in the reduced bond strength of $Co(III)^- O^{2-}/OH$.[93–95] A weak M–O bond between the B-site cation and the oxygen adsorbate directly affects the breakup of the adsorbate to regenerate OH– for continuing the ORR. Similarly, Otagawa et al. reported an inverse correlation between the B-site cation-adsorbate bond strength and the OER activity for spinel transition metal oxides.[96] DFT studies suggested that a coordination of three sulfur atoms per Ni(II) in spinel nickel sulfides maximizes the ORR performance, applicable to those surface Ni(II).[97] Generally, a lower ORR activation energy is found for metal centers with a moderate coordination number. This is because at a high coordination number the proton transfer to the oxygen adsorbate on the active metal center would be almost fully blocked off by steric hindrance, while with low coordination numbers few active sites are available to bond the hydroxide adsorbate.[98] Another factor

benefitting the high catalytic activity is the synergistic coupling between cobalt and nickel sulfides, which sometimes even takes place in their mechanical mixtures. For instance, a solid-state mixture of NiS_2 and CoS_2 delivered an ORR current density 10 times that of the individual NiS_2 or CoS_2 at a potential of 0.8 V vs. RHE.[99]

The three nickel cobalt sulfide catalysts were further deposited onto carbon papers to form air-cathodes, and evaluated in secondary Zn–air batteries, using Pt/C, RuO_2, or a 50–50 mixture of Pt/C and RuO_2 as the benchmark catalyst. Fig. 6a shows the charge–discharge profiles of the zinc–air batteries using one of the three nickel cobalt sulfides or NiS_2 based air-cathodes. Clearly, the battery with the NC11-based air-cathode outperformed the rest by a lower charge voltage and a higher discharge voltage at almost all tested current densities. Despite a similar performance to that of the batteries made with the considered benchmark catalysts on air-cathodes at moderate current densities (<50 mA cm^{-2}), the NC11-based battery becomes the superior one as soon as the current density rises across 75 mA cm^{-2} (Fig. 6b), a better rate performance more desirable for practical energy storage applications.
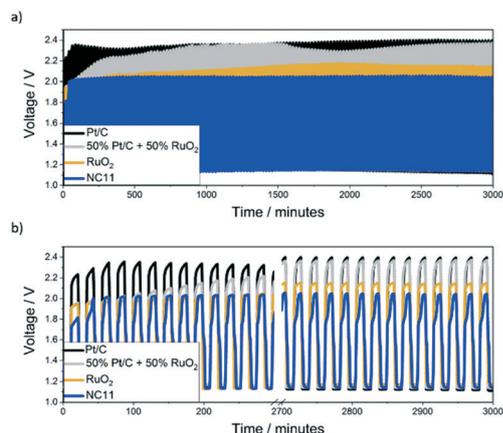
The power density of the zinc–air batteries with the NC11-based air electrode was up to 87 mW cm^{-2} at a current density of 150 mA cm^{-2}, higher than that of batteries with RuO_2-based air electrodes. It is also higher or on a par with those of zinc–air batteries with air cathodes made from a number of bifunctional catalysts, such as Co_3O_4/stainless steel,[100] carbon black/MnO_2,[101] and MnO_2–$LaNiO_3$/carbon nanotube (CNT).[102] The power density may be further improved by engineering the morphology of the catalysts or incorporating conductive supports. For instance, a porous hollow $NiCo_2S_4$ microsphere based air-cathode achieved a power density of 130 mW at 150 mA cm^{-2}.[8] With the high conductivity and large electrochemically active surface area provided by the N-doped CNT network support, $NiCo_2S_4$ mounted thereon was even able to deliver 148 mW cm^{-2} at 250 mA cm^{-2}.[71] However, with varied battery structure, exposed catalyst area and catalyst loading across studies, inter-study comparisons are only of qualitative significance.

The Nyquist plots in Fig. 6d suggest a higher impedance for NC11 compared to Pt/C and RuO_2, which is likely due to its poorer contact to the carbon additives. Lower resistance is often observed for catalysts directly grown on current collectors.[4] Among the three nickel cobalt sulfides, NC31 and NC11 showed clear advantages over NC13 which are likely a result of their higher conductivity. To facilitate a more detailed understanding, three-component equivalent circuits were fitted for all three plots, revealing a descending order of resistance of NC13 > NC11 > NC13 (Fig. S4a†), in agreement with our discussion above on the conductivity of these catalysts. Moreover, the double-layer capacitance (CdI, see ESI† S4b) of our materials was determined to be 8.402 mF, 6.238 mF, and 4.491 mF for NC11, NC13, and NC31, respectively. The CdI values have been shown to be linearly correlated with the electrochemically active surface area
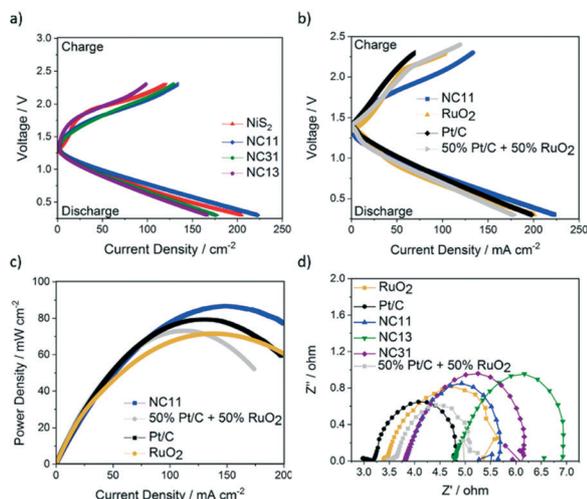
Fig. 6 Performance of Zn–air batteries with the air-cathode made from nickel cobalt sulfides, RuO_2, or Pt/C. a) Galvanostatic charge–discharge curves of the nickel cobalt sulfides and NiS_2. b) Galvanostatic charge-density curves of batteries using NC11, RuO_2, Pt/C, or a 50–50 mixture of Pt/C and RuO_2 in the air-cathode. c) Power density plots derived from the galvanodynamic discharge curves. d) Nyquist plot obtained from electrochemical impedance spectroscopy of Zn–air batteries made with nickel cobalt sulfides, RuO_2, Pt/C. or a 50–50 mixture of Pt/C and RuO_2.

This journal is © The Royal Society of Chemistry 2020

Catal. Sci. Technol., 2020, 10, 2173–2182 | 2179

Fig. 7 a) Cycling stability testing data of the batteries with air-cathodes made of NC11, Pt/C, RuO$_2$, or a 50–50 mixture of Pt/C and RuO$_2$. The galvanostatic pulse cycling tests were conducted at 4 mA cm^{-2} with a discharge and charge period of 12 min each per cycle. b) Voltage range comparison for the first and last 300 min.

(ECSA) in the literature, particularly for materials of similar composition.[103] Interestingly, the increase in CdI is accompanied by an increase in nickel concentration, specifically Ni(III), which has also been suggested in the literature.[104] However, the increase in CdI alone is not responsible for the improved performance of our nickel cobalt sulfide materials: NC13, which possesses a 39% higher CdI value than NC31, only exhibits a *ca.* 6% improvement in discharge current density. In contrast, NC11, which possesses a 87% higher CdI value than NC31, exhibits a *ca.* 34% improvement in discharge current density, significantly higher than expected based on the ECSA alone, suggesting that a strong cationic contribution is present.

Zinc–air batteries with air-cathodes made of NC11, Pt/C, and RuO$_2$ were subjected to continuous and repetitive charge and discharge at 4 mA cm^{-2} (Fig. 7). The NC11-based battery survived over 3500 min, or approximately 125 cycles. The initial discharge and charge voltages were 1.15 and 2.02 V, respectively, similar to or better than those of batteries based on Pt/C (1.19 and 2.23 V), RuO$_2$ (1.12 and 1.98 V), or a 50–50 mixture of Pt/C and RuO$_2$ (1.18 and 2.10 V). The NC11-based battery continued to give an almost constant charge and discharge voltage for 100 cycles, but slightly degraded to 1.13 and 2.04 V for discharge and charge by the end of the 125th cycle, as evidenced by the voltage gap broadening of 0.04 V, in the range 0.87 to 0.91 V. In sharp contrast, the voltage gap broadening by cell deterioration was tripled (0.12 V in the range 0.86 to 0.98 V) for the RuO$_2$-based battery, and 6 times (0.26 V in the range 1.04 to 1.30 V) for the Pt/C-based battery, with the 50–50 mixture exhibiting the highest level of broadening (0.31 V in the range 1.14 to 2.37 V). The steady voltages of the NC11-based battery account for its high levels of energy efficiency and bifunctional catalytic activity, which lowers the overpotentials in the respective processes. A lower overpotential in turn slows down the catalyst degradation and eventual deactivation, improving the cell-life.[8] The

discharge voltages for all the batteries are *ca.* 1.2 V, which is fairly decent. The lowest charge voltage (1.96 V) for the NC11-based battery leads to the highest energy efficiency, showing the superiority of NC11 as a bifunctional catalyst for rechargeable zinc–air batteries.

Conclusions

Spinel nickel cobalt sulfides produced *via* a CHFS process were evaluated as catalysts for the OER and ORR, and subsequently as air-electrode catalyst materials in secondary zinc–air batteries. It was established that the zinc–air battery with the air-cathode containing nickel cobalt sulfide exhibited a power density of 87 mW cm^{-2} at a current density of 150 mA cm^{-2}, outperforming batteries utilizing RuO$_2$ in their air cathodes. A high Ni(III) content was found to improve the OER activity, while a high content of Ni(II) and Co(II) was believed to improve the ORR activity. NC11-based zinc–air batteries showed excellent stability, with only 1 to 2% deterioration in discharge and charge voltages over 125 cycles. This study deepens the understanding on the roles of nickel and cobalt cations in the oxygen electrocatalysis process, which could aid future design of spinel-type electrocatalysts for desired high performance. The industrial scale-up CHFS process makes it possible for this study to help advance the development of high-performance catalysts for the construction of reliable and high-energy zinc–air batteries on the commercial scale. Future studies on nickel cobalt sulfides may focus on tailoring morphological attributes and doping to maximize their catalytic performances. Furthermore, a deeper understanding of long-term stability should be obtained, through post-cycling characterization studies. Finally, to facilitate a holistic understanding of the cation's contribution to catalytic processes, carefully designed computational simulation (DFT) work would need to be undertaken.

Conflicts of interest

The authors declare no conflict of interest for this work.

Acknowledgements

2180 | *Catal. Sci. Technol.*, 2020, **10**, 2173–2182

This journal is © The Royal Society of Chemistry 2020

References

1 M. Pablo-Romero, R. Pozo-Barajas and R. Yñiguez, *Energy Policy*, 2017, **101**, 342–352.
2 D. Larcher and J.-M. Tarascon, *Nat. Chem.*, 2015, **7**, 19.
3 Y. Li and H. Dai, *Chem. Soc. Rev.*, 2014, **43**, 5257–5275.
4 A. Sumboja, X. Ge, F. Goh, B. Li, D. Geng, T. Hor, Y. Zong and Z. Liu, *ChemPlusChem*, 2015, **80**, 1341–1346.
5 A. Sivanantham, P. Ganesan and S. Shanmugam, *Adv. Funct. Mater.*, 2016, **26**, 4661–4672.
6 Q. Liu, J. Jin and J. Zhang, *ACS Appl. Mater. Interfaces*, 2013, **5**, 5002–5008.
7 X. Wu, S. Li, B. Wang, J. Liu and M. Yu, *New J. Chem.*, 2017, **41**, 115–125.
8 M. Wang, Y. Lai, J. Fang, F. Qin, Z. Zhang, J. Li and K. Zhang, *Catal. Sci. Technol.*, 2016, **6**, 434–437.
9 D. Liu, Q. Lu, Y. Luo, X. Sun and A. M. Asiri, *Nanoscale*, 2015, **7**, 15122–15126.
10 W. Xu, Z. Lu, X. Lei, Y. Li and X. Sun, *Phys. Chem. Chem. Phys.*, 2014, **16**, 20402–20405.
11 A. Sumboja, J. Chen, Y. Zong, P. S. Lee and Z. Liu, *Nanoscale*, 2017, **9**, 774–780.
12 Z. Zhang, X. Wang, G. Cui, A. Zhang, X. Zhou, H. Xu and L. Gu, *Nanoscale*, 2014, **6**, 3540–3544.
13 F. Lai, D. Yong, X. Ning, B. Pan, Y. E. Miao and T. Liu, *Small*, 2017, **13**, 1602866.
14 Y. Pan, Y. Lin, Y. Chen, Y. Liu and C. Liu, *J. Mater. Chem. A*, 2016, **4**, 4745–4754.
15 M. Lübke, A. Sumboja, L. McCafferty, C. F. Armer, A. D. Handoko, Y. Du, K. McColl, F. Cora, D. Brett and Z. Liu, *ChemistrySelect*, 2018, **3**, 2613–2622.
16 K. Ojha, S. Saha, B. Kumar, K. S. Hazra and A. K. Ganguli, *ChemCatChem*, 2016, **8**, 1218–1225.
17 J. Wu, S. Dou, A. Shen, X. Wang, Z. Ma, C. Ouyang and S. Wang, *J. Mater. Chem. A*, 2014, **2**, 20990–20995.
18 M. Sun, J. Tie, Y. Li and L. Yu, *Gen. Chem.*, 2017, **3**, 202–206.
19 F. F. Tao, J.-j. Shan, L. Nguyen, Z. Wang, S. Zhang, L. Zhang, Z. Wu, W. Huang, S. Zeng and P. Hu, *Nat. Commun.*, 2015, **6**, 7798.
20 C. Xia, P. Li, A. Gandi, U. Schwingenschlögl and H. Alshareef, *Chem. Mater.*, 2015, **27**, 6482–6485.
21 L. Hou, L. Hua, R. Bao, Z. Chen, C. Yang, S. Zhu, G. Pang, L. Tong, C. Yuan and X. Zhang, *ChemPlusChem*, 2016, **81**, 557–563.
22 D. P. Dubal, P. Gomez-Romero, B. R. Sankapal and R. Holze, *Nano Energy*, 2015, **11**, 377–399.
23 Z. Wu, Y. Zhu and X. Ji, *J. Mater. Chem. A*, 2014, **2**, 14759–14772.
24 X. Xu, W. Liu, Y. Kim and J. Cho, *Nano Today*, 2014, **9**, 604–630.
25 M.-R. Gao, Y.-F. Xu, J. Jiang and S.-H. Yu, *Chem. Soc. Rev.*, 2013, **42**, 2986–3017.
26 J. Xiao, X. Zeng, W. Chen, F. Xiao and S. Wang, *Chem. Commun.*, 2013, **49**, 11734–11736.
27 J.-Y. Lin and S.-W. Chou, *Electrochem. Commun.*, 2013, **37**, 11–14.
28 Y. Xue, Z. Zuo, Y. Li, H. Liu and Y. Li, *Small*, 2017, **13**, 1700936.
29 L. Ma, Y. Hu, R. Chen, G. Zhu, T. Chen, H. Lv, Y. Wang, J. Liang, H. Liu and C. Yan, *Nano Energy*, 2016, **24**, 139–147.
30 J. Jiang, C. Yan, X. Zhao, H. Luo, Z. Xue and T. Mu, *Green Chem.*, 2017, **19**, 3023–3031.
31 X. Y. Yu, L. Yu and X. W. D. Lou, *Adv. Energy Mater.*, 2016, **6**.
32 Z. Ai, Z. Hu, Y. Liu and M. Yao, *ChemPlusChem*, 2016, **81**, 322–328.
33 F. Deng, J. Tie, B. Lan, M. Sun, S. Peng, S. Deng, B. Li, W. Sun and L. Yu, *Electrochim. Acta*, 2015, **176**, 359–368.
34 A. Pramanik, S. Maiti, M. Sreemany and S. Mahanty, *Electrochim. Acta*, 2016, **213**, 672–679.
35 Y. Zhu, X. Chen, W. Zhou, K. Xiang, W. Hu and H. Chen, *Electrochim. Acta*, 2017, **249**, 64–71.
36 J. Shen, J. Ji, P. Dong, R. Baines, Z. Zhang, P. M. Ajayan and M. Ye, *J. Mater. Chem. A*, 2016, **4**, 8844–8850.
37 G. He, M. Qiao, W. Li, Y. Lu, T. Zhao, R. Zou, B. Li, J. A. Darr, J. Hu and M. M. Titirici, *Adv. Sci.*, 2017, **4**, 1600214.
38 B. Lu, D. Cao, P. Wang, G. Wang and Y. Gao, *Int. J. Hydrogen Energy*, 2011, **36**, 72–78.
39 J.-P. Jacobs, A. Maltha, J. G. Reintjes, J. Drimal, V. Ponec and H. H. Brongersma, *J. Catal.*, 1994, **147**, 294–300.
40 W. King and A. Tseung, *Electrochim. Acta*, 1974, **19**, 493–498.
41 I. Nikolov, R. Darkaoui, E. Zhecheva, R. Stoyanova, N. Dimitrov and T. Vitanov, *J. Electroanal. Chem.*, 1997, **429**, 157–168.
42 G. Li, M. A. Mezaal, K. Zhang and L. Lei, *Int. J. Electrochem. Sci.*, 2015, **10**, 5395–5404.
43 J. A. Darr, J. Zhang, N. M. Makwana and X. Weng, *Chem. Rev.*, 2017, **117**, 11125–11238.
44 O. Cech, P. Vanysek, L. Chladil and K. Castkova, *ECS Trans.*, 2016, **74**, 331–337.
45 T. Adschiri, K. Kanazawa and K. Arai, *J. Am. Ceram. Soc.*, 1992, **75**, 1019–1022.
46 C. Xu, J. Lee and A. S. Teja, *J. Supercrit. Fluids*, 2008, **44**, 92–97.
47 Z. Zhang, J. B. M. Goodall, D. J. Morgan, S. Brown, R. J. H. Clark, J. C. Knowles, N. J. Mordan, J. R. G. Evans, A. F. Carley, M. Bowker and J. A. Darr, *J. Eur. Ceram. Soc.*, 2009, **29**, 2343–2353.
48 P. W. Dunne, A. S. Munn, C. L. Starkey, T. A. Huddle and E. H. Lester, *Philos. Trans. R. Soc., A*, 2015, **373**, 20150015.
49 X. Weng, P. Boldrin, I. Abrahams, S. J. Skinner and J. A. Darr, *Chem. Mater.*, 2007, **19**, 4382–4384.
50 R. Q. C. C. J. Tighe, R. I. Gruar and J. A. Darr, *Ind. Eng. Chem. Res.*, 2013, **16**, 5522–5528.
51 A. K. H. P. Boldrin, A. A. Chaudhry, L. Otley, B. Theibaut, P. Bishop and J. A. Darr, *Ind. Eng. Chem. Res.*, 2007, **46**, 4830–4838.
52 C. J. T. R. I. Gruar and J. A. Darr, *Ind. Eng. Chem. Res.*, 2013, **52**, 5270–5281.
53 X. Weng, P. Boldrin, Z. Zhang and J. Darr, *Clean Technology 2008: Bio Energy, Renewables, Green Building, Smart Grid, Storage, and Water*, 2008, pp. 261–264.

This journal is © The Royal Society of Chemistry 2020

Catal. Sci. Technol., 2020, **10**, 2173–2182 | **2181**

54 M. J. Powell, P. Marchand, C. J. Denis, J. C. Bear, J. A. Darr and I. P. Parkin, *Nanoscale*, 2015, **7**, 18686–18693.

55 J. Darr, C. J. Tighe and R. Gruar, *US Pat.*, 9192901, 2015.

56 X. Weng, J. Zhang, Z. Wu, Y. Liu, H. Wang and J. A. Darr, *Appl. Catal., A*, 2011, **103**, 453–461.

57 M. Lübke, I. Johnson, N. M. Makwana, D. Brett, P. Shearing, Z. Liu and J. A. Darr, *J. Mater. Chem. A*, 2015, 22908–22914.

58 R. I. Gruar, C. J. Tighe, P. Southern, Q. A. Pankhurst and J. A. Darr, *Ind. Eng. Chem. Res.*, 2015, **54**, 7436–7451.

59 Y. Tao, L. Ruiyi and L. Zaijun, *Mater. Lett.*, 2016, **167**, 234–237.

60 A. Ashok, A. Kumar, J. Ponraj, S. A. Mansour and F. Tarlochan, *Int. J. Hydrogen Energy*, 2019, **44**, 16603–16614.

61 O. Knop, K. Reid, Sutarno and Y. Nakagawa, *Can. J. Chem.*, 1968, **46**, 3463–3476.

62 X. Zhang and A. Zunger, *Adv. Funct. Mater.*, 2010, **20**, 1944–1952.

63 D. Kim, G. Ghodake, N. Maile, A. Kadam, D. Lee, V. Fulari and S. Shinde, *Sci. Rep.*, 2017, **7**, 9764.

64 K. Liang, W. He, X. Deng, H. Ma and X. Xu, *J. Alloys Compd.*, 2018, **735**, 1395–1401.

65 X. Chen, D. Chen, X. Guo, R. Wang and H. Zhang, *ACS Appl. Mater. Interfaces*, 2017, **9**, 18774–18781.

66 J. Suntivich, K. J. May, H. A. Gasteiger, J. B. Goodenough and Y. Shao-Horn, *Science*, 2011, **334**, 1383–1385.

67 A. Grimaud, K. J. May, C. E. Carlton, Y.-L. Lee, M. Risch, W. T. Hong, J. Zhou and Y. Shao-Horn, *Nat. Commun.*, 2013, **4**, 2439.

68 H. Tanaka and M. Misono, *Curr. Opin. Solid State Mater. Sci.*, 2001, **5**, 381–387.

69 L. Zhang, H. Zhang, L. Jin, B. Zhang, F. Liu, H. Su, F. Chun, Q. Li, J. Peng and W. Yang, *RSC Adv.*, 2016, **6**, 50209–50216.

70 J. Liu, J. Wang, B. Zhang, Y. Ruan, L. Lv, X. Ji, K. Xu, L. Miao and J. Jiang, *ACS Appl. Mater. Interfaces*, 2017, **9**, 15364–15372.

71 X. Han, X. Wu, C. Zhong, Y. Deng, N. Zhao and W. Hu, *Nano Energy*, 2017, **31**, 541–550.

72 J. Li, W. Xu, J. Luo, D. Zhou, D. Zhang, L. Wei, P. Xu and D. Yuan, *Nano-Micro Lett.*, 2018, **10**, 6.

73 Z. Kang, H. Guo, J. Wu, X. Sun, Z. Zhang, Q. Liao, S. Zhang, H. Si, P. Wu and L. Wang, *Adv. Funct. Mater.*, 2019, **29**, 1807031.

74 M. Li, Y. Xiong, X. Liu, X. Bo, Y. Zhang, C. Han and L. Guo, *Nanoscale*, 2015, **7**, 8920–8930.

75 R. Singh, J. Pandey, N. Singh, B. Lal, P. Chartier and J.-F. Koenig, *Electrochim. Acta*, 2000, **45**, 1911–1919.

76 Y. Liang, Y. Li, H. Wang, J. Zhou, J. Wang, T. Regier and H. Dai, *Nat. Mater.*, 2011, **10**, 780.

77 M. Jahan, Z. Liu and K. P. Loh, *Adv. Funct. Mater.*, 2013, **23**, 5363–5372.

78 C. Tang, N. Cheng, Z. Pu, W. Xing and X. Sun, *Angew. Chem.*, 2015, **127**, 9483–9487.

79 J. Fu, Z. P. Cano, M. G. Park, A. Yu, M. Fowler and Z. Chen, *Adv. Mater.*, 2017, **29**, 1604685.

80 E. Fabbri, R. Mohamed, P. Levecque, O. Conrad, R. Kötz and T. Schmidt, *ChemElectroChem*, 2014, **1**, 338–342.

81 X. Yu, T. Hua, X. Liu, Z. Yan, P. Xu and P. Du, *ACS Appl. Mater. Interfaces*, 2014, **6**, 15395–15402.

82 W. Fu, C. Zhao, W. Han, Y. Liu, H. Zhao, Y. Ma and E. Xie, *J. Mater. Chem. A*, 2015, **3**, 10492–10497.

83 X. Wu, S. Li, B. Wang, J. Liu and M. Yu, *Phys. Chem. Chem. Phys.*, 2017, **19**, 11554–11562.

84 J. Xiao, L. Wan, S. Yang, F. Xiao and S. Wang, *Nano Lett.*, 2014, **14**, 831–838.

85 X. Li, Q. Li, Y. Wu, M. Rui and H. Zeng, *ACS Appl. Mater. Interfaces*, 2015, **7**, 19316–19323.

86 H. Y. Wang, Y. Y. Hsu, R. Chen, T. S. Chan, H. M. Chen and B. Liu, *Adv. Energy Mater.*, 2015, 5.

87 Z. Liu, N. Li, H. Zhao, Y. Zhang, Y. Huang, Z. Yin and Y. Du, *Chem. Sci.*, 2017, **8**, 3211–3217.

88 X. Gao, X. Long, H. Yu, X. Pan and Z. Yi, *J. Electrochem. Soc.*, 2017, **164**, H307–H310.

89 M. Hamdani, R. Singh and P. Chartier, *Int. J. Electrochem. Sci.*, 2010, **5**, 556–577.

90 L. Yu, L. Zhang, H. B. Wu and X. W. D. Lou, *Angew. Chem.*, 2014, **126**, 3785–3788.

91 J. Suntivich, H. A. Gasteiger, N. Yabuuchi, H. Nakanishi, J. B. Goodenough and Y. Shao-Horn, *Nat. Chem.*, 2011, **3**, 546.

92 C. Wei, Z. Feng, G. G. Scherer, J. Barber, Y. Shao-Horn and Z. J. Xu, *Adv. Mater.*, 2017, **29**, 1606800.

93 D. Kan, Y. Orikasa, K. Nitta, H. Tanida, R. Kurosaki, T. Nishimura, T. Sasaki, H. Guo, Y. Ozaki and Y. Uchimoto, *J. Phys. Chem. C*, 2016, **120**, 6006–6010.

94 A. Aijaz, J. Masa, C. Rösler, W. Xia, P. Weide, A. Botz, R. Fischer, W. Schuhmann and M. Muhler, *Angew. Chem., Int. Ed.*, 2016, **55**, 4087–4091.

95 H. Wang, R. Liu, Y. Li, X. Lü, Q. Wang, S. Zhao, K. Yuan, Z. Cui, X. Li and S. Xin, *Joule*, 2017, 337–348.

96 J. O. Bockris and T. Otagawa, *J. Phys. Chem.*, 1983, **87**, 2960–2971.

97 B. Yan, D. Krishnamurthy, C. H. Hendon, S. Deshpande, Y. Surendranath and V. Viswanathan, *Joule*, 2017, **1**, 600–612.

98 J. Nørskov, J. Rossmeisl, A. Logadottir, L. Lindqvist, J. Kitchin, T. Bligaard and H. Jonsson, *J. Phys. Chem. B.*, 2004, **108**, 17886–17892.

99 L. Zhu, D. Susac, M. Teo, K. Wong, P. Wong, R. Parsons, D. Bizzotto, K. Mitchell and S. Campbell, *J. Catal.*, 2008, **258**, 235–242.

100 D. U. Lee, J. Y. Choi, K. Feng, H. W. Park and Z. Chen, *Adv. Energy Mater.*, 2014, **4**, 1301389.

101 C. Z. Luo, Y. Zhu, Y. Xu, Y. Liu, T. Gao, J. Wang and C. Wang, *J. Power Sources*, 2014, **250**, 372–378.

102 H. Ma and B. Wang, *RSC Adv.*, 2014, **4**, 46084–46092.

103 X.-Z. Song, F.-F. Sun, Y.-L. Meng, Z.-W. Wang, Q.-F. Su and Z. Tan, *New J. Chem.*, 2019, **43**, 3601–3608.

104 A. Zhang, R. He, H. Li, Y. Chen, T. Kong, K. Li, H. Ju, J. Zhu, W. Zhu and J. Zeng, *Angew. Chem., Int. Ed.*, 2018, **57**, 10954–10958.

2182 | *Catal. Sci. Technol.*, 2020, **10**, 2173–2182

This journal is © The Royal Society of Chemistry 2020